2007

Integrating laboratory creep compaction data with numerical fault models: A Bayesian framework

Delphine D. Fitzenz
Ecole et Observatoire des Sciences de la Terre

André Jalobeanu
Laboratoire des Sciences de l'Images

Stephen H. Hickman
U.S. Geological Survey

JOURNAL OF GEOPHYSICAL RESEARCH, VOL. 112, B08410, doi:10.1029/2006JB004792, 2007

Integrating laboratory creep compaction data with numerical fault models: A Bayesian framework

Delphine D. Fitzenz,[1] André Jalobeanu,[2] and Stephen H. Hickman[3]

Received 10 October 2006; revised 12 April 2007; accepted 26 April 2007; published 14 August 2007.

[1] We developed a robust Bayesian inversion scheme to plan and analyze laboratory creep compaction experiments. We chose a simple creep law that features the main parameters of interest when trying to identify rate-controlling mechanisms from experimental data. By integrating the chosen creep law or an approximation thereof, one can use all the data, either simultaneously or in overlapping subsets, thus making more complete use of the experiment data and propagating statistical variations in the data through to the final rate constants. Despite the nonlinearity of the problem, with this technique one can retrieve accurate estimates of both the stress exponent and the activation energy, even when the porosity time series data are noisy. Whereas adding observation points and/or experiments reduces the uncertainty on all parameters, enlarging the range of temperature or effective stress significantly reduces the covariance between stress exponent and activation energy. We apply this methodology to hydrothermal creep compaction data on quartz to obtain a quantitative, semiempirical law for fault zone compaction in the interseismic period. Incorporating this law into a simple direct rupture model, we find marginal distributions of the time to failure that are robust with respect to errors in the initial fault zone porosity.

Citation: Fitzenz, D. D., A. Jalobeanu, and S. H. Hickman (2007), Integrating laboratory creep compaction data with numerical fault models: A Bayesian framework, *J. Geophys. Res.*, *112*, B08410, doi:10.1029/2006JB004792.

1. Introduction

[2] When analyzing rock deformation experimental data, one deals with both measurement errors and complexity in the deformation processes. This often leads to partial or only qualitative data analyses, which limits the application of these studies to large-scale geophysical problems (e.g., modeling of the earthquake source). To bridge the gap between laboratory studies and their application, there is a need for a probabilistic approach that can be used both to infer the parameters of a constitutive model from experimental rock compaction data, and to simulate numerically the time-dependent porosity reduction in fault zones from a known (e.g., lab-derived) constitutive relationship, while still keeping track of all the uncertainties. This latter step is crucial if we are to achieve process-based seismic hazard assessment. Both the rate of effective stress buildup (namely, due to fault compaction) and the recovery of fault strength between earthquakes determine how long it will take for different parts of the previously ruptured fault to reach failure again, thus controlling the timing and the size of the next rupture [*Segall and Rice*, 1995]. Although laboratory compaction and time-dependent strength recovery data are key elements in obtaining a physical understanding of this process [*Muhuri et al.*, 2003], deterministic fault models derived from these data need a measure of their robustness if they are to be useful in generating forecasts of earthquake rupture timing and extent. It is therefore important to work within a modeling framework that enables the use and propagation of uncertainties in the experimental data and the model parameters through to the final result.

[3] Toward this end, we present here a probabilistic, Bayesian, framework for the analysis of laboratory compaction data. Our approach is illustrated by a directed graphical model. Though not commonly used in the Earth Sciences, graphical models are very useful to show the relationships between all the variables, parameters, observations and models that play a role in a given (direct or inverse) problem. We show how the experimental setup can be represented in such a model, and how this enables us to decompose, in a rigorous fashion, the inversion of the creep data. Because we are mainly interested in deformation mechanisms that can play a role in the interseismic compaction of fault zones, we focus on one rather simple, though experimentally derived, compaction law that we consider valid for a range of diffusion-controlled mechanisms. Its parameters are a stress exponent, an apparent activation energy, and a porosity term. However, the approach presented here could accommodate any other type of mechanism.

[4] We first develop the method for the general case of time-dependent porosity reduction during hydrostatic com-

[1] Institut de Physique du Globe, Ecole et Observatoire des Sciences de la Terre, Strasbourg, France.
[2] Laboratoire des Sciences de l'Images, de l'Informatique et de la Télédétection, Strasbourg, France.
[3] U.S. Geological Survey, Menlo Park, California, USA.

0148-0227/07/2006JB004792$09.00

paction at hydrothermal conditions and show how it can be used to decide on the optimal range of experimental parameters (temperature, effective stress, etc.) and the number of tests needed to generate a robust suite of constitutive parameters (stress exponent, apparent activation energy, porosity term). We then adapt this Bayesian inference method to determine these constitutive parameters from experimental creep compaction data on quartz obtained at elevated temperatures by *Niemeijer et al.* [2002]. Finally, we show how the creep laws so derived can be implemented in direct (generative) models of the time evolution of porosity and fluid pressure along faults during the earthquake cycle, using graphical models as a guide to propagate experimental uncertainties. This approach represents a substantial improvement over existing fault zone compaction models, which utilize arbitrary compaction laws with little or no basis in laboratory experiments [see *Fitzenz and Miller*, 2003].

2. Application of Bayesian Inference to Time-Dependent Compaction

[5] The Bayesian methodology is an approach to statistics in which all forms of uncertainty are expressed in terms of probability [*Bernardo and Smith*, 1994]. Indeed, geophysical field data, experimental lab results or any piece of information, no matter how obtained, can be described by probabilities in the case of discrete variables or by a probability density function (pdf), in the case of continuous variables. In this study, we consider random variables, some of which are linked by deterministic models. This differs greatly from the pure deterministic modeling approaches; instead of yielding single values, this method will yield probability density functions for all the model results. Given this probabilistic approach, forward calculations are distinguished from forward modeling and referred to as generative modeling, and the inverse calculations are not called an inversion anymore, but a Bayesian inference.

[6] In the present study, we develop a Bayesian inference method specifically to analyze laboratory compaction experiments performed on natural and synthetic fault gouge samples. To do so, we chose a simple and rather general creep compaction law, and then fit this creep law to a set of experimentally derived porosity time series. Since porosity in a general compaction creep law can exhibit a highly nonlinear dependence on effective stress and temperature, our method consists of (1) finding an optimal parameterization, providing a behavior as linear as possible over a finite range of stress and temperature, and (2) then performing whatever inference is required to solve for the constitutive parameters in the original (physically meaningful) creep law. This is a fundamentally different approach than is commonly used in analysis of creep compaction data, in which all but one of the independent variables (e.g., compaction strain, effective stress, temperature, grain size) are held fixed in an experiment while the remaining variable is systematically changed to solve for the dependence of compaction rate on that free variable. In addition to the computation of the covariance matrix, the main advantage of our method compared to common practice is the fact that we integrate the creep rate law with respect to time and can deal with porosity as a function of time or ''compacted porosity'' as a function of initial porosity if the time interval is fixed. This removes three difficulties encountered in traditional analyses of laboratory compaction data: (1) the choice of a relevant definition for the ''state'' of a sample, (2) the small number of data points effectively used in the analysis due to the need to compare strain rates for samples at the same state, and (3) the large uncertainties associated with the computed derivatives of the porosity or strain versus time curves when the deformation rate is low (i.e., typically, when the ratio between the instantaneous and the starting porosity becomes lower than 0.5 [*Niemeijer et al.*, 2002]).

[7] To show how this analysis can be used in forward modeling of fault compaction, we also propose a simple generative model of Coulomb failure for an undrained fault compacting following the creep law inferred from the data of *Niemeijer et al.* [2002]. This enables us to discuss the shape of the pdfs both for the time to failure and for the stress and porosity conditions at failure which depends not only on the covariance matrix of the creep parameters but also on the pdf of the initial porosity (or of any other parameter).

3. Inferring Creep Parameters From Measurements of Time-Dependent Compaction

[8] The rationale for and the full description of the methodology used here are given by *Fitzenz et al.* [2005] for the more general case of repeated porosity measurements (e.g., from field or borehole, direct or indirect observations). For completeness, we present here a short summary of the method as applied to analysis of porosity versus time data from laboratory compaction experiments.

3.1. Choice of the Creep Law

[9] The creep behavior of rocks depends on temperature (T), pressure (P), the presence or absence of fluids, and the mineralogy and grain size distribution of the rock assemblage. Experimental compaction studies have been carried out on a wide variety of materials, including halite [*Spiers et al.*, 1990; *Hickman and Evans*, 1992; *Bos et al.*, 2000] and quartz [e.g., *Schutjens*, 1991; *Dewers and Hajash*, 1995; *Chester et al.*, 2004]. Many processes were shown to be active at hydrothermal conditions, especially in polycrystalline compaction experiments, including intergranular pressure solution, cataclasis rate-limited by subcritical crack growth, and intracrystalline plasticity [*Bos et al.*, 2000; *Dewers and Hajash*, 1995; *Schutjens*, 1991; *Chester et al.*, 2004]. In many cases, the interpretation of the experimental data was made difficult because the data did not fit the theoretical laws well, owing to a transition in rate-controlling deformation mechanisms during the experiments, complex mineralogy, changes in grain packing geometry, or other effects that were not included in the theoretical rate laws. In other cases, the range of T, P conditions employed in these experiments were insufficient to yield a well-constrained constitutive relationship [*Chester et al.*, 2004]. Even when a good fit of data to the rate laws was obtained, in all cases the data were analyzed ''independently'' for the different parameters of the laws (as described in section 2), and the uncertainties were not evaluated at each step and propagated to the next, making

it difficult to use the derived creep laws in quantitative numerical models and assess the robustness of their results. Therefore, although there is a wealth of experimental data obtained for rock creep that gives us valuable insights into the deformation mechanisms involved and their relative sensitivities to variations in T, P, mineralogy, grain size, fluid chemistry and other factors, creep laws deriving from quantitative analyses of these data are scarce.

[10] Most theoretical compaction laws are tailored to a single deformation mechanism (dislocation creep, intergranular pressure solution, cataclastic flow, stress corrosion cracking) and are characterized by a stress exponent, an activation energy, a porosity term, and another term, usually dependent on the grain size. However, during deformation of real fault gouges, more than one process can be occurring at a given time (maybe over different timescales) and a single-mechanism rate law is probably not appropriate. We therefore choose to invert creep data for a more general creep law of the form [*Rutter and Wanten*, 2000]

$$\dot{\phi} = \theta_0 \, \sigma_{\text{eff}}^{\theta_1} \exp(-\theta_2/(RT)) \exp(\theta_3 \phi) \tag{1}$$

giving the porosity reduction rate as a function of the effective confining stress (σ_{eff}), temperature (T in °K), and instantaneous porosity (ϕ). In this expression, θ_1 is the stress exponent, θ_2 is the activation energy, and θ_3 is an empirically derived porosity term. θ_0 is an empirical constant, containing the grain size sensitivity, which will be assumed constant in section 4 where we analyze experiments conducted at roughly constant grain size.

[11] In the experiments analyzed here [*Niemeijer et al.*, 2002], each porosity measurement (in %) is determined to an accuracy of ±1 to 2%. We assume that this corresponds to a 95% confidence interval and represent the overall measurement error in porosity as a Gaussian, with standard deviation 0.5%. Here, porosity is treated as a bulk property of the sample, i.e., spatial variations of porosity within the sample are ignored. In the following, we evaluate the probability density function (pdf) of the parameters of the general creep law (i.e., equation (1), which we will call the model) knowing the porosity as a function of time at different T and σ_{eff} conditions.

[12] Although we use only one "model," one could test different creep laws. In particular, once θ_1 and θ_2 in equation (1) are determined, one could propose a probable dominant mechanism and try the same inversion scheme for more appropriate (i.e., physically based) creep laws. Indeed, the Bayesian framework is a natural framework for model selection and assessment, allowing for the determination of the best creep law for a particular experimental data set.

3.2. Hierarchical Bayesian Formulation of the Inference Scheme

3.2.1. Background and Graphical Model

[13] The relationships between all the ingredients of our problem are synthesized in a directed graphical model (Figure 1). In such a model, each node represents a set of random variables. A black arrow pointing from node A to node B means that B depends on A (or that B can be derived using A, or that A causes B). In terms of probability, it denotes a conditional pdf. The terminal nodes without incoming arrows are prior pdfs. They represent what we believe to be true before starting the experiments (i.e., the a priori assumptions). The least restrictive startup point for the initial porosity in our case is a uniform pdf between 0 and 100%. The multidimensional pdf of all the variables (i.e., joint pdf) is then given by the product of all prior and conditional pdfs according to the graph structure. What we want is to find the best parameters for a given model and a given data set (i.e., take the arrows backward, or follow the thick arrows on the graph). In other words, we want to find the parameter values that maximize the posterior pdf of the creep parameters. According to Bayes' theorem, it is equivalent to maximizing this joint probability. This is called Bayesian estimation [see *Bernardo and Smith*, 1994].

[14] To mimic realistic circumstances, we show the relationships between the variables for a set of i observations of (time-dependent) porosity for each one of the n temperature and effective stress conditions (i.e., n experiments). The factorial structure of the graph is due to the experimental design. Sets of i observations and n experiments are symbolized by rectangles or plates [*Jordan*, 2004].

[15] In other words, the graph on Figure 1 means that the noisy ϕ_{obs} derive from (i.e., are conditionally dependent upon) the time t of the measurement, the inferred initial porosity (φ_0) and the experimental temperature and stress conditions by using model m and its parameters θ. It means that if we have a creep model and know its parameters, we just need to choose the temperature and stress conditions and an initial porosity to simulate creep experiments. In the direct (black arrow) sense, the graph is therefore called a generative model. On the contrary, if the sense of the arrows is reversed (thick arrows), the graph maps out the different steps needed to perform the Bayesian inference. Starting from the (inherently noisy) observations of porosity as a function of time during creep experiments, it aims at computing the distribution of the creep parameters that best explains the data, assuming that model m is true.

[16] Note that although φ_0 might be measured for some of the experiments, it is meant here as a model parameter inferred from the analysis of all the porosity measurements at $t \geq 0$ for a given experiment. The accuracy of this parameter (with uncertainties) estimated this way is indeed much greater than by using one measurement. The standard deviation for the observed porosities has to be defined for each experiment. This way, we can account for varying data quality, in particular when extreme values of temperature and stresses are investigated. In principle, all the nodes (except the model) are random variables. Since temperature, stresses and time are determined much more accurately than porosities, we simplify the problem, and assume that they can be known perfectly (fixed values). We will also assume that the porosity measurements follow a Gaussian distribution due to measurement uncertainties.

[17] The mathematical derivation is only outlined in section 3.2.2 and is presented in detail in Appendix A.

3.2.2. Direct and Inverse Approaches: Equations

[18] Because we are using a creep law of the form of equation (1), the compacted porosity ϕ as a function of the porosity prior to compaction φ_0 is given by

$$\phi = f(\varphi_0, t) = -\frac{1}{\theta_3} \log(\theta_3 \, t \, \gamma' + e^{-\alpha \varphi_0}) \tag{2}$$

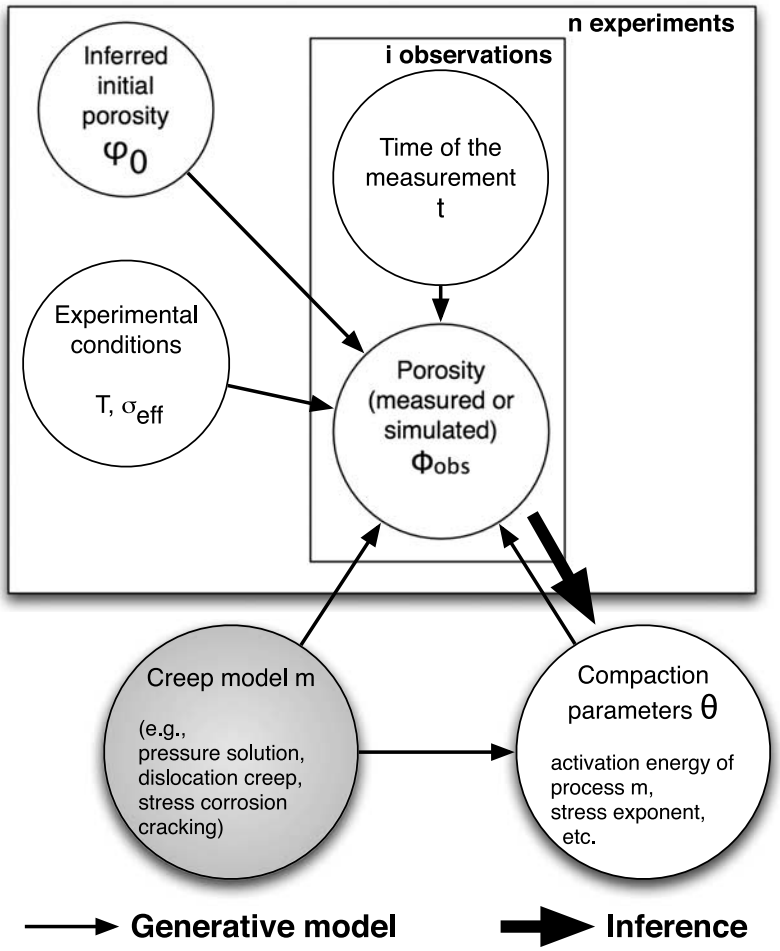

Figure 1. Simplest graphical model representing the creep compaction experiments. All the white nodes are random variables. The black arrows show the dependence between them. This graph means that noisy ϕ_{obs} derive from the time t of the measure, the inferred initial porosity φ_0, and the experimental temperature and stress conditions, by using model m and its parameters θ. The thick arrow represents the inference step. The inference starts from the (inherently noisy) observations of porosity as a function of time during creep experiments and aims at computing the distribution of the creep parameters that best explains the data, assuming that model m is true.

where

$$\gamma' = -\theta_0 \, \sigma_{\text{eff}}^{\theta_1} \, e^{-\theta_2/(RT)} \tag{3}$$

where t is the time since the onset of compaction and φ_0 is the initial porosity. Note that in our previous analysis [*Fitzenz et al.*, 2005] the time interval between successive measurements of compacted porosity was assumed constant and $f(\varphi, \Delta t)$ was a function of $\gamma = \gamma' \Delta t$.

[19] First, we need to reparameterize the problem, since it is highly nonlinear [*MacKay*, 1998]. This consists of finding an optimal parameterization, having a behavior as linear as possible, performing whatever inference is required, and finally going back to the original parameterization (equation (2)). In contrast to the case of successive porosity measurements where no initial porosity can be defined for the whole data set and where the time interval between measurements is constant [*Fitzenz et al.*, 2005], the parameterization has to be adapted to account for the fact that the duration of the compaction interval changes between each observation and between experiments.

[20] Figure 2 shows the corresponding graphical model, wherein the problem was decomposed into as many elements as needed to have the simplest possible relationships between the variables used in our analysis. This makes both the choice of the algorithm and the expression of the corresponding probabilities much easier. Time, temperature, and effective stress are now assumed perfectly known (fixed), and porosity is decomposed as an ideal porosity ϕ resulting from equation (2), and an observed (noisy) porosity ϕ_{obs} of mean ϕ. Spatial variabilities of porosity within the samples are ignored.

[21] Since there are now more nodes (variables) on the graph than just the data and the parameters we want to infer, we first need to integrate the joint pdf over all possible values of the variables we are not interested in. This is called a marginalization step. In our case, these variables include the initial porosity for each experiment, as well as the intermediate random variables λ', ν, and Θ that were

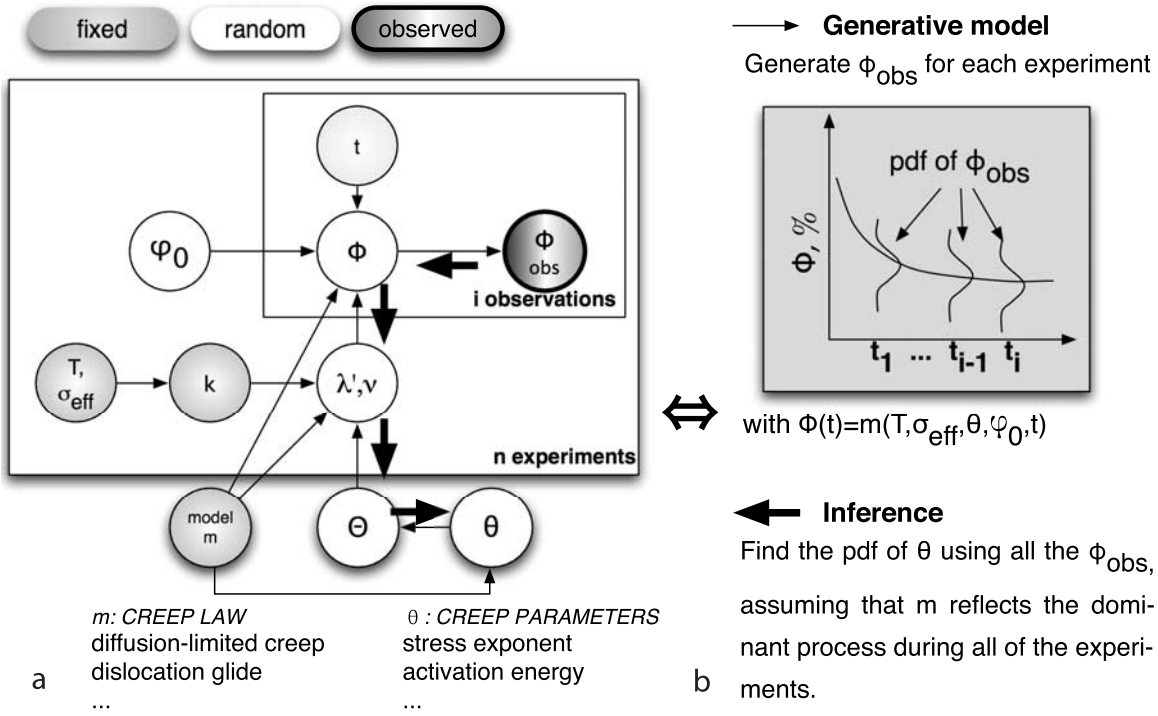

Figure 2. Detailed graphical model for the inference. The thin arrows indicate that the noisy ϕ_{obs} can be generated from (i.e., are conditionally dependent upon) the exact compacted porosity ϕ at time t as computed for each initial porosity φ_0 and experimental setup by using model m and its parameters θ. In contrast to this approach, the inference starts from the (inherently noisy) observations of porosity as a function of time during creep experiments and aims at computing the distribution of creep parameters that best explains the data, assuming that model m is true (thick arrows). The intermediate random variables λ', ν, and Θ were introduced only to make the problem more linear (i.e., easier to solve).

introduced only to make the problem more linear (i.e., easier to solve), as will be explained in this section. Because of the complexity of the problem, we use a hierarchical approach in conducting the inference of constitutive parameters. In step A, each one of the n experiments is treated individually before proceeding to the final estimation of the parameters. Indeed, in a "1 to n" tree structure, we can perform an independent inference on the tree branches. This is why we introduce the n parameters ν in the graphical model (Figure 2), which are the estimates of μ for each experiment. Thus, after step A is completed, we have n joint posterior pdfs of (λ', ν) knowing the observations $\{\phi^i_{\text{obs}}\}$. In step B we infer the parameters Θ using these posterior pdfs as "observations." This is equivalent to the message passing algorithm [*Jordan and Weiss*, 2002]. Last, we revert to the original θ and compute the covariance matrix between the creep parameters using the Jacobian matrix of the transform between $\{\Theta\}$ and $\{\theta\}$.

[22] If one is only interested in a subset of the parameters θ, the related distribution is simply obtained by keeping the corresponding entries of the covariance matrix $\Sigma = (J^T B J)^{-1}$; this will be used in section 4.

3.3. Performing the Inference on Simulated Compaction Data: A Planning Tool

[23] We model compaction numerically using the solution f to the creep law (equation (5)). Such a creep law was empirically derived by *Rutter and Wanten* [2000] from a suite of experiments performed on synthetic mixtures of quartz sand in a matrix of fine grained illite + muscovite. In these experiments, the samples were hydrostatically compacted at a range of effective pressures between 10 MPa and 210 MPa, with a constant pore water pressure of 70 MPa and temperatures ranging between 300 and 450°C (i.e., between 573 and 723°K).

[24] We use equation (2) with the parameters listed as "true" in Table 1 to compute the porosity time series for three different series of simulated experiments (settings): (1) six experiments, T from 300°K to 420°K and σ_{eff} from 15 to 105 MPa; (2) 12 experiments, same range of T and σ_{eff}; (3) 12 experiments, T from 300°K to 720°K and σ_{eff} from 15 to 200 MPa. All simulated experiments were run for both 20 and 50 data points per experiment (cases a and b, respectively). The purpose of this simulation is to illustrate the effect of increasing (1) the number of experiments, (2) the number of data points acquired per experiment, or (3) changing the range of temperatures and effective stresses investigated in these experiments on the accuracy with which constitutive parameters for creep compaction can be determined. We start with an arbitrary initial porosity of 27%, and we choose increasing time intervals as the (simulated) experiments progress. The time intervals between two consecutive data points correspond to a porosity variation of 0.8% for the 20-point experiments and 0.5% for the 50-point experiments. Finally, we add Gaussian noise to the porosity with a standard deviation of

Table 1. Inference Results for Three Simulated Experimental Settings Compared to the True Values of the $\{\theta\}$ Parameters[a]

Experimental Setting	Result Type	Case	θ_0, $MPa^{-\theta_1}\ s^{-1}$	θ_1	θ_2, kJ mol^{-1}	θ_3	Correlation Coefficients (θ_1, θ_2)
All	true value		2.6×10^{-7}	3.13	114.5	0.73	0
1	optimum	a	1.32×10^{-7}	3.17	115	0.76	0.44
		b	1.46×10^{-7}	3.23	115.2	0.75	0.56
	marginal SD	a	3.8×10^{-8}	0.06	0.63	0.007	
		b	2.7×10^{-8}	0.05	0.55	0.004	
2	optimum	a	1.27×10^{-7}	3.16	115.5	0.77	0.48
		b	1.89×10^{-7}	3.11	114.5	0.75	0.54
	marginal SD	a	3.13×10^{-8}	0.04	0.68	0.006	
		b	2.9×10^{-8}	0.03	0.50	0.003	
3	optimum	a	1×10^{-7}	3.15	114.8	0.77	0.03
		b	1.80×10^{-7}	3.13	114.6	0.75	0.14
	marginal SD	a	1.9×10^{-8}	0.02	0.28	0.006	
		b	1.6×10^{-8}	0.02	0.21	0.003	

[a]See text. Case a refers to 20 data point experiments whereas case b refers to 50 data point experiments. SD, standard deviation.

0.5% to simulate intrinsic uncertainties in laboratory data acquisition.

[25] The results are given in Table 1 for settings 1, 2, and 3, for both 20 and 50 data points per experiment. The absolute agreement between the stress exponent (θ_1) and the activation energy (θ_2) inferred from the simulations versus the true values is best for setting 3, intermediate for setting 2 and worst for setting 1, but only by relatively small amounts. In addition, the marginal standard deviations are systematically smaller for the 50-point cases than for the 20-point cases. As expected, this indicates that we recover these constitutive parameters most accurately by using the greater number of experiments over a wider range of temperatures and effective stresses.

[26] More significantly, we can compare the correlation coefficients (ratio between the covariance and the square root of the product of the variances) between the activation energy and stress exponent inferred from our analyses. They are shown in Table 1. The correlation coefficients are about 0.5 for the four first sets of simulated experiments (1 a and b and 2 a and b); uncertainty is essentially the same regardless of the number of points per experiment or the number of experiments for a given range of T and σ_{eff}. However, the correlation coefficients decrease dramatically below 0.15 when the range of T and σ_{eff} is increased (setting 3 a and b). This situation is further illustrated by the corresponding 95% confidence regions for the activation energy and stress exponent shown on Figure 3, at both 20 (Figure 3, left) and 50 (Figure 3, right) data points per experiment.

[27] *Rutter and Wanten* [2000] report that the wet phyllosilicate + quartz sand experiments showed significantly more compaction than any of their control experiments (dry sand, dry sand + phyllosilicate, and wet clean sand). The corresponding petrographic analysis showed interpenetration of grain contacts, formation of quartz overgrowths, a decrease in the amount of quartz embedded in the phyllosilicate matrix, and an increase in mean grain size of quartz with progressive compaction. They attributed these effects to solution and redeposition of quartz. For such fluid-assisted compaction processes, we expect the apparent activation energy to be essentially independent of stress, as represented by equation (1). In this case, θ_1 and θ_2 are independent variables and should be uncorrelated. Thus the lower correlation coefficient for experimental setting 3 indicates that it is preferable to the other two settings, showing that a greater range of temperature and stress is preferable for independently resolving the stress exponent and the activation energy. In contrast, the correlation coefficients for settings 1 and 2 are relatively large and similar, indicating that increasing the number of experiments, while covering the same range of pressure and temperature conditions, will not reduce the correlation significantly. Finally, increasing the number of data points per experiment from 20 to 50 (see Figures 2a and 2b) maintains a similar

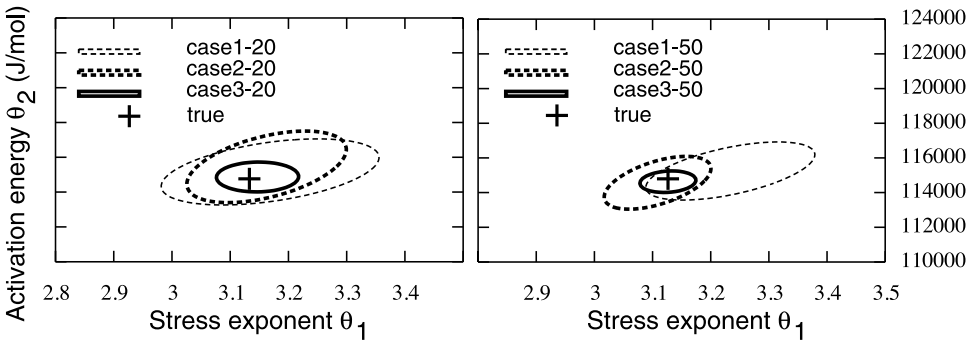

Figure 3. The 95% confidence regions for the stress exponent and the apparent activation energy derived for the three settings (Table 1) with (left) 20 and (right) 50 data points.

Table 2. Description of the Five Experiments Used in the Inference[a]

Sample	Confining Pressure, MPa	Fluid Pressure, MPa	Temperature, K	Final Grain Size, μm	Initial Porosity, %
CPf3	300	200	773	47.1	27.31
CPf4	300	150	773	42.9	29.39
CPf5	300	250	773	40.5	26.12
CPf6	300	200	673	40.9	25.14
CPf7	300	200	873	43.2	31.38

[a]Derived from Table 1 of *Niemeijer et al.* [2002].

covariance but results in a dramatic decrease in the experimental uncertainties for each parameter (i.e., the size of the corresponding error ellipse is dramatically reduced).

[28] In summary, increasing the range of temperature and effective stress conditions in an experiment is clearly desirable as it enables one to reduce the covariance between the inferred constitutive parameters, whereas having more experiments and more data points per experiment reduces the uncertainties in these constitutive parameters. Were a large correlation to be obtained despite these precautions, it would be very useful information since it could indicate a change in the dominant deformation mechanism during the course of the experiments. This could be elucidated by performing the same inference but on different time windows. For other types of creep deformation processes (e.g., dislocation creep), such analyses would need to be performed with the appropriate candidate creep laws, which would have greatly different forms than equation (1).

4. Application of This Analysis to Actual Creep Compaction Experiments

[29] We present an application of this analysis to isotropically stressed water-saturated drained compaction experiments on quartz sand samples by *Niemeijer et al.* [2002]. In these experiments (Table 2), temperatures ranged between 400 and 600°C, confining pressure was 300 MPa, and fluid pressures ranged between 150 and 250 MPa. The porosity ranged from 30% down to 10%. We use data from their experiments Cpf3 to Cpf7, all with final grain sizes between 40.5 and 47.1 μm, so that we can ignore grain size effects on compaction rates.

4.1. Inversion of the Global Data Set

[30] For each of the *Niemeijer et al.* [2002] experiments, there are from 15 to 19 measurements of porosity, for a total of 88 (t, ϕ) data points. We analyzed these data by performing step A for each experiment and then step B, as described in section 3.

[31] Through this analysis, we find $\theta_0 = 6.40 \times 10^{-11}$ $MPa^{-\theta}0$ s^{-1}; the stress exponent (θ_1) = 2.55; an apparent activation energy (θ_2) = 37 kJ mol^{-1}; the porosity term (θ_3) = 0.53, with standard deviations of 3.0×10^{-11} $MPa^{-\theta 0}$ s^{-1}, 6.2×10^{-2}, 1.6 kJ mol^{-1}, and 9.4×10^{-3}, respectively. The covariance between the activation energy and stress exponent is very small, with a correlation coefficient of 0.16, as illustrated by the confidence ellipses in Figure 4.

[32] These results are very different from those obtained by *Niemeijer et al.* [2002] using more traditional analysis techniques (outlined in section 4.2). They find a stress exponent of 3.09 ± 0.17 and an apparent activation energy between 60 and 85 kJ mol^{-1}. In section 4.2 we show why these two different analyses led to such divergent results.

4.2. Restricting the Range of Analyzed Data to Better Target Rate-Controlling Processes

[33] *Niemeijer et al.* [2002] used the ratio between the instantaneous porosity at time t and the porosity at the onset of the experiment as a proxy for the state of the sample, using the following methodology. First, they measured porosity as a function of time and, from that, computed the volumetric strain rate using the two-point central difference method. They then fit straight lines through log(strain rate) versus ϕ/ϕ_0 data for each experiment and interpolated or extrapolated these strain rate curves to evaluate strain rate at constant ϕ/ϕ_0 (their proxy for constant state) under a variety of temperature and pressure conditions. Then they computed the slopes of $\log_{10}$(strain rate) versus $\log_{10}$(effective stress) to derive the stress exponent and that of log (strain rate) versus 1000/RT to estimate the apparent activation energy, for five values of ϕ/ϕ_0 ranging from 0.5 to 0.9. At each state, they had to rely on only two to three points to compute the slope, because there are only three experiments for which T was kept constant while the effective stress was varied, and three other experiments for which the effective stress was fixed and the temperature varied. Finally, they took the average of the stress exponent

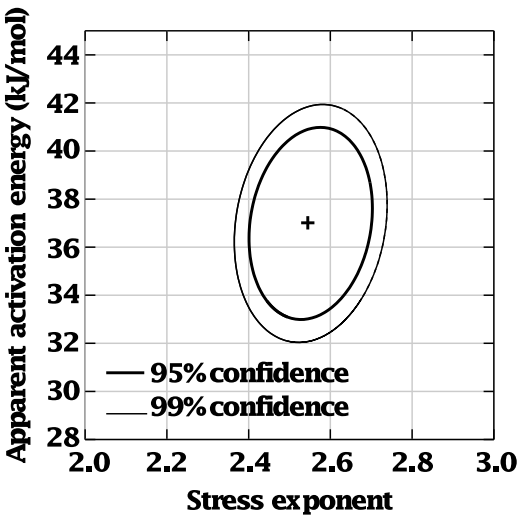

Figure 4. The 95% and 99% confidence regions for the stress exponent and the apparent activation energy derived from the global *Niemeijer et al.* [2002] data set. Note that the axes of the ellipse are almost parallel to the axes of the graph, denoting a very small correlation between the two variables.

Table 3. Results of the Inference Performed on the *Niemeijer et al.* [2002] Data Set Restricted to $0.5 \leq \phi/\phi_0 \leq 0.8$[a]

Optimal Values	θ_0, $MPa^{-\theta 0}\ s^{-1}$	θ_1	θ_2, kJ mol^{-1}	θ_3	
	4.20E-13	3.56	57.63	0.72	
Covariance matrix	5.59E-26	−2.35E-14	−2.19E-10	−3.02E-15	θ_0
	-	1.22E-02	1.98E+02	1.58E-03	θ_1
	-	-	6.72E+06	3.44E+01	θ_2
	-	-	-	2.74e-04	θ_3

[a]The covariance matrix is symmetric by definition. Read 5.59E-26 as 5.59×10^{-26}.

and apparent activation energy determined for all five values of ϕ/ϕ_0.

[34] *Niemeijer et al.* [2002] found that in the beginning of their experiments, the stress exponents and the apparent activation energy both increase from 3.35 to 3.58 and from 65 to 85 kJ mol^{-1}, respectively, when ϕ/ϕ_0 decreases from 0.9 to 0.7 but that for $\phi/\phi_0 = 0.6$, the apparent activation energy is about 62 kJ mol^{-1} and the stress exponent is decreased to 2.3. This might indicate that the rate-controlling process changes during the experiment, or that there are poorly controlled changes in packing geometry or other state variables that complicate their (and our) interpretation of constitutive parameters.

[35] To see if we can reconcile the divergent constitutive parameters obtained by our different approaches, we checked how the results of our inversion change when we analyze subsets of the data over discrete domains of the state variable ϕ/ϕ_0. If we take only the first eight data points for each experiment (roughly $\phi/\phi_0 \geq 0.8$), we get an apparent activation energy of 23 kJ mol^{-1}. If we take the seven first points ($\phi/\phi_0 \geq 0.9$), we get 8.8 kJ mol^{-1}. In this latter case, seven points per experiment make 35 points total used in our analysis, to be compared with the three points used by *Niemeijer et al.* [2002] to constrain activation energy. However, in both cases, these values are likely to reflect only the early deformation due to the injection of water into the sample to reach the desired pore pressure (C. Spiers, personal communication, 2006). In addition, there was a sudden decrease in strain rate for these experiments at $\phi/\phi_0 \leq 0.5$, possibly due to the dissolution of copper from the sample capsule or to a change in controlling mechanism [*Niemeijer et al.*, 2002].

[36] We therefore analyzed the ''middle'' part of the *Niemeijer et al.* [2002] data set (i.e., points for which $0.5 \leq \phi/\phi_0 \leq 0.8$). In this case, the residuals (difference between predicted and measured porosities) are much smaller than for the global inversion. Applying our Bayesian inference method to this subset, we get an activation energy in the range of 49.50 to 66.00 kJ mol^{-1} (99% confidence interval) with an optimal value of 57.6 kJ mol^{-1} (Table 3 and Figure 5). This range includes the 65.0 kJ mol^{-1} that *Niemeijer et al.* [2002] find for $\phi/\phi_0 = 0.6$ and is not too far from the 75.0 kJ mol^{-1} that they found for $\phi/\phi_0 = 0.8$. We also get a stress exponent in the range of 3.23 to 3.90 (99% confidence interval) with a preferred value of 3.56. This range includes the 3.45 and 3.58 values found by *Niemeijer et al.* [2002] for $\phi/\phi_0 = 0.8$ and 0.7, respectively. As expected, the confidence ellipses we obtain are much larger for the subset than for the global inference (see Figures 4 and 5), due to the reduced number of data points used (52) in the latter case. The axes of these ellipses are oblique, indicative of a significant correlation (0.66) as computed from the covariance matrix determined through our analysis (Table 3). Please note that errors for the constitutive parameters obtained by *Niemeijer et al.* [2002] for each value of ϕ/ϕ_0 are difficult to assess since they are related to the residuals, which are poorly defined for small data populations. Indeed, this measure of the uncertainty strongly depends on the number of data points, and in the extreme case of two data points, the apparent error reduces to 0.

[37] In conclusion, there may be several competing deformation mechanisms occurring during the course of the *Niemeijer et al.* [2002] experiments that lead to variable and state-dependent constitutive parameters that are not adequately accounted for in their (or our) constitutive model. Most published studies on rock deformation in the laboratory aim to find the most probable processes and their rate-controlling mechanisms as a first step toward developing a constitutive law. This is usually done by performing a data analysis following a methodology similar to that of *Niemeijer et al.* [2002]. The experiments are technological challenges and take a long time. However, once the results are found to be roughly reproducible, the search for the apparent activation energy and the stress exponent rely only on a small fraction of the data points collected. Furthermore, the values obtained for these constitutive parameters (and their uncertainties) typically do not include the experimental fluctuations observed in the porosity time series from one sample to another at exactly the same conditions. What we propose in this study is a robust inversion technique for the same ''effective'' or apparent parameters. This technique allows the use of all the data, either simultaneously or in

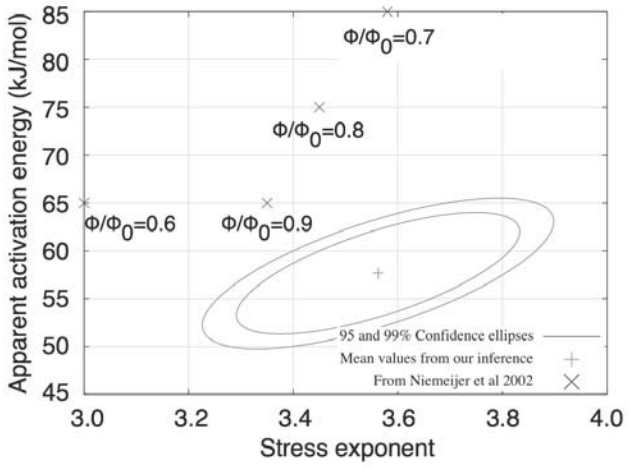

Figure 5. The 95% and 99% confidence regions for the stress exponent and the apparent activation energy derived from the *Niemeijer et al.* [2002] data set restricted to ϕ/ϕ_0 between 0.5 and 0.8. The axes of the ellipses are now at an angle to the axes of the graph; that is, the correlation between the two variables is now significant (0.66). Also note that the uncertainties (i.e., size of the ellipses) are larger than on Figure 4. The crosses refer to the results by *Niemeijer et al.* [2002] at the indicated porosity ratios ϕ/ϕ_0.

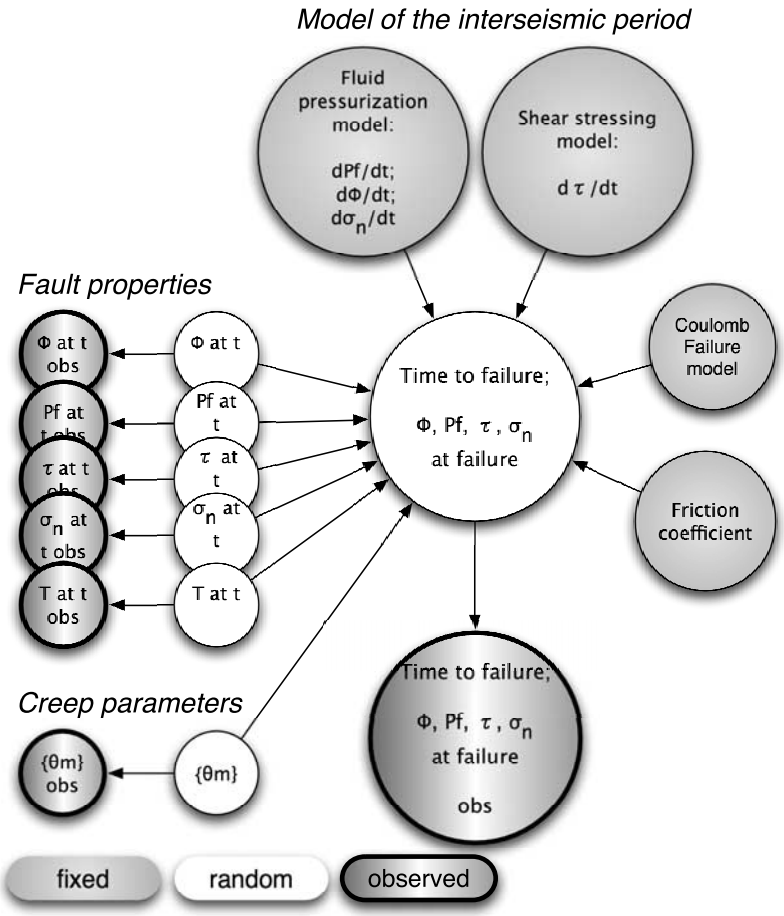

Figure 6. Generative model used to compute the time to failure and the porosity and stress conditions at failure. The pdfs for the input parameters are discussed in the text. No a priori assumptions are made regarding the form of the pdfs for time to failure; t is the time measured right after an earthquake.

overlapping subsets (i.e., sliding windows), thus making more complete use of the experimental data and propagating statistical variations in the data through to the final rate constants.

[38] An interesting follow-up to this study would be to choose a series of creep laws based on different grain-scale deformation mechanisms and perform the inference again for each of these laws. We could then compare the evidence (that is, the pdf of the data, knowing the model [*MacKay*, 2003, Chapter 28]) for each model, and choose the model that best describes the data as a way of more rigorously identifying the rate-controlling mechanism. Again, such a model selection could not be made with the usual inversion method.

[39] The simple creep model used here does not capture all the physics and chemistry at play. Extrapolation outside of the range of T and σ_{eff} conditions investigated in a particular suite of experiments without the basis of a microphysical model would therefore be hazardous. The inference scheme that we propose can nonetheless give robust estimates of the main effective parameters for relevant ϕ/ϕ_0 intervals, under conditions comparable to those investigated in the laboratory. It is our belief that such "empirical" quantitative laws could already be used as a proxy for more physically based constitutive laws in forward models of interseismic compaction and pore pressure evolution in fault zones. In section 5, we present a first application of this type, and discuss the results in terms of marginal probability densities for the time to failure and stresses and porosity at failure.

5. Integration of the Derived Creep Law Into a Fault Zone Compaction Model: Forward Approach

5.1. Principles of the Method

[40] We show here an example of integration of lab data into a model for the time-dependent compaction-driven pore pressure buildup within a porous fault zone. For illustrative purposes, we will use the empirical compaction creep law derived in section 4 from the *Niemeijer et al.* [2002] data as a constitutive law.

[41] We chose a very simple case in which only one fault element is considered, but of course future applications could add a number of adjacent and/or interacting fault elements as well as more realistic fault zone mineralogies as new laboratory data become available.

[42] The graphical model (Figure 6) shows the various ingredients contained in our model computing the time to failure of a fault element. The nodes of the graph are the

porosity ϕ_t and the stress conditions (normal stress, shear stress, pore pressure) at time t; the temperature (T); the static friction coefficient; and finally the creep parameters $\{\theta_m\}$. Additional model inputs are provided by the fluid pressurization model, which describes coupled creep compaction and fluid flow in the porous fault zone, the shear stressing model, which describes the rate of increase in shear stress resolved onto the fault due to plate motions or postseismic relaxation, and the failure model, which defines the critical resolved shear stress on the fault at failure according to the Coulomb criterion. All of these inputs help determine the time to failure, and the ϕ and stress conditions at failure. The time evolution of the resistance to failure only stems from that of the pore pressure.

[43] Time t is measured after an earthquake and we consider the fault properties immediately after rupture to depend mostly on the dynamics of the rupture rather than on the previous interseismic period. Therefore they are stochastically independent from the interseismic creep parameters.

[44] For simplicity, we assume here that the fault is undrained and compacts following the creep law inferred from our preceding analysis of the *Niemeijer et al.* [2002] data (see section 5.2 for more discussion), and that T and the static friction coefficient are constant with time. We further assume that the normal stress is constant and that shear stress increases linearly with time. We solve the coupled differential equations giving the porosity reduction rate and the fluid mass conservation using a Runge-Kutta fourth-order integration scheme. Poroelasticity or time-dependent normal stress could be introduced easily into this scheme, but are not included in the present analysis. The rupture criterion is $\tau \geq$ coefficient of friction $\times$ $(\sigma_n - P_f)$, with friction equal to 0.6 [after *Byerlee*, 1978].

[45] Simply put, we have introduced a stochastic element (through the parameters of the creep law) to an otherwise uniform loading system and this will add random variability to failure times. With such nonlinear problems, it is difficult to predict the nature of the stochastic process and how it affects the pdf of time to failure.

[46] Before engaging into the mathematically and computer intensive task of finding the joint pdfs and the covariance matrix of the results, we first check the shape of the marginal probability distributions of the results. To do so, we use the Bayesian network of Figure 6 to build a generative model and we sample the input parameter space using a Monte Carlo sampling technique. We generate a large number (here 80,000) of samples of θ_m and compute histograms of time to failure and P_f and τ at failure. What we want to achieve here is different than in the inference sections. In this direct problem, we want to know how the marginal distributions of the time to failure and properties at failure are affected by the randomness of the input parameters, including the compaction parameters and the initial porosity (or, e.g., the shear stress increase rate). In this manner, we check if the parameter space in which we are operating is the optimal one in which to solve the problem. We also check the relative influence of uncertainties in the other parameters (e.g., the porosity at time t) on the shape and width of the histograms by generating samples of ϕ_t.

[47] This study differs from traditional Coulomb failure stress studies in three main ways. First, interseismic fluid pressurization within the fault zone (assumed undrained, here) is explicitly addressed. Second, the creep law used in this modeling results from a quantitative analysis of a suite of lab experiments, i.e., is explicitly lab-derived. Also, finally, instead of yielding a mean time to failure, our modeling produces the whole distribution of possible times to failure and fault properties at the onset of failure. Finally, we would like to emphasize that the shape of those probability density functions are not chosen arbitrarily before we start the modeling, but rather derive directly from the distributions of the creep parameters which proved to be Gaussian close to their optimum values and from the set of deterministic relationships that link all the model ingredients. In other words, the shape of the pdf for time to failure that we obtain in this section directly reflects the physics we put into our modeling.

5.2. Choice of the Creep Parameters

[48] When we analyzed the *Niemeijer et al.* [2002] data, we found two posterior probability density functions for the creep parameters with very different properties. For the analysis of the global data set, for the reasons discussed in section 4.2, the results are deemed less representative of true creep compaction than those for subsets of the data. However, the stress exponent and activation energy were uncorrelated and were determined with more accuracy. On the other hand, the creep parameters inferred from the subset for $0.5 \leq \phi/\phi_0 \leq 0.8$ are deemed more realistic but the correlation coefficient of the stress exponent and the apparent activation energy is 0.7 (instead of 0.16 in the former case) and the marginal standard deviation of each parameter is larger.

[49] In the following, we will first describe the method and show results using the well-determined, though less physically meaningful creep parameters for the entire *Niemeijer et al.* [2002] data set. Then we will show how the shape of the marginal distribution of the time to failure is affected by the use of the creep parameters derived from the subset of data for $0.5 \leq \phi/\phi_0 \leq 0.8$. Obviously, what we want to use is a well determined posterior pdf of the creep parameters whose optimal values are most physically meaningful.

5.3. Tests for Fixed and Random Initial Porosities

[50] In order to perform these tests, we chose a depth of 3 km, a normal stress equal to the lithostatic stress (for a rock density of 2750 kg m^{-3}), a hydrostatic initial pore pressure, and a temperature corresponding to a thermal gradient of 30°K km^{-1} [*Williams et al.*, 2004]. The initial shear stress is 20 MPa and the shear stress increase rate is 8×10^{-3} Pa s (2.5 bars yr^{-1}). This is a relatively high stressing rate (inferred 0.15 bar yr^{-1} for the North Anatolian Fault [*Stein et al.*, 1997]) and is meant to represent an upper limit (see discussion in section 6.2).

[51] The creep parameters were determined in sections 4.1 and 4.2 for the entire *Niemeijer et al.* [2002] data set as a multivariate Gaussian distribution, defined by a mean (vector θ_{opt}) and a covariance matrix (Σ). Although the creep law is deemed most relevant to temperatures and stresses comparable to those investigated during the experiments, we use our model to extrapolate these experimental results to shallow conditions (i.e., lower temperatures) so that our point source fault model can mimic the occurrence of

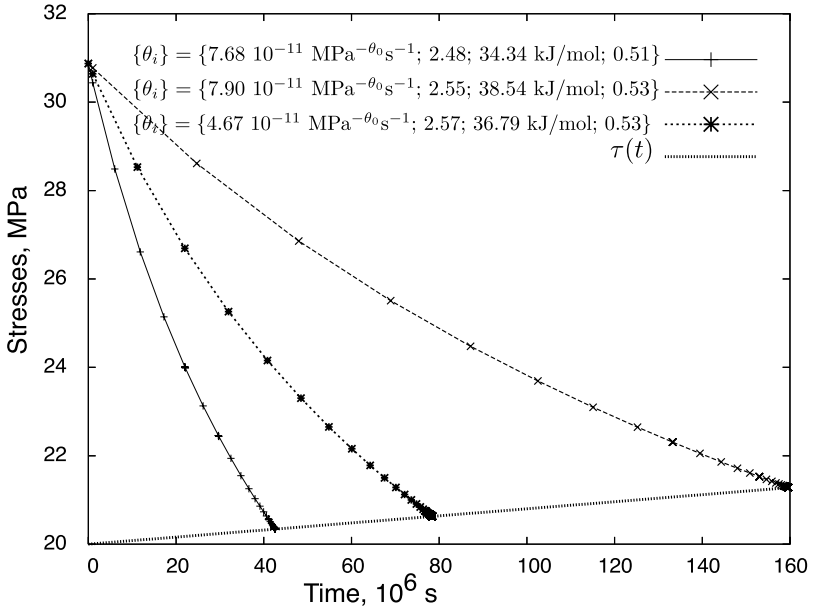

Figure 7. Computation of the time to failure for three samples of $\{\theta\}$ drawn from the pdfs obtained by inference. The straight line shows the shear stress resolved on the fault, and the three curves show the time evolution of the fault shear strength, friction coefficient $\times$ $(\sigma_n - P_f)$. The times to failure are the intersections between the line and the curves, following the Coulomb criterion. The quantities in braces are for θ_0, the stress exponent θ_1, the apparent activation energy θ_2, and the porosity term θ_3.

shallow microearthquakes, such as observed at Parkfield, CA.

[52] To draw a random vector θ from the four-dimensional Gaussian distribution, we first compute the Cholesky decomposition (matrix square root) of Σ (i.e., we find the unique lower triangular matrix A such that $AA^T = \Sigma$). Let $Z = (z_1, .., z_4)$ be a vector whose components are four independent standard normal variables (which can be generated, for example, by using the Box-Muller transform). Then $\theta = \theta_{opt} + A\ Z$.

[53] In an undrained system, the pore pressure evolution can be computed by numerically integrating the coupled differential equations

$$\frac{\partial \varphi}{\partial t} = \theta_0 \left(\sigma_n - P_f\right)^{\theta_1} e^{-\theta_2/RT}\, e^{\theta_3 \varphi} \tag{4}$$

$$\frac{\partial P_f}{\partial t} = -\frac{\partial \varphi}{\partial t}\frac{1}{\varphi \beta}, \tag{5}$$

where σ_n is the normal stress (taken here as equal to the constant lithostatic stress) and β is the bulk compressibility of the fault element (fluid and porous matrix).

[54] In Figure 7, we show the time evolution of fault strength (coefficient of friction $\times$ $(\sigma_n - P_f)$) and the shear stress resolved on the fault for three sets of creep parameters $\{\theta\}$. The intersections between the strength curves and the shear stress curve define the corresponding three times to failure. These three sets of parameters $\{\theta\}$ were not arbitrarily chosen but are rather three samples drawn from the multivariate pdf found in our previous analysis of the global [*Niemeijer et al.*, 2002] data set. The initial porosity (ϕ_t) is 12%. In these examples the pore pressures at failure are very close to each other for the three different creep laws, owing to the relatively slow rate of shear stress increase relative to compaction rate. In other words, the term friction coefficient $\times$ $(\sigma_n - P_f)$ is between 20 and 22 MPa for all three cases. However, these differences are enhanced when translated into time to failure because of the slower shear stress increase rate. Since the shear loading rate that we chose is in fact rather large (2.5 bars yr^{-1}), even for plate boundary faults, we can note that our model yields very rapid fluid pressurization when the fault zones are sealed (undrained).

[55] Using the Cholesky decomposition method described above, we generated 80,000 samples of θ from the posterior pdf obtained by our Bayesian analysis of the global data set of *Niemeijer et al.* [2002] (i.e., with optimal values of $\{\theta_j\}$ = 6.4×10^{-11}, 2.55, 37, 0.53). Figure 8 displays the corresponding histograms of the input constitutive parameters (Figure 8, top) and of the model results for time to failure, and porosity, shear stress and pore pressure at failure (Figure 8, bottom). First, we note that although pdfs for the input parameters are symmetric (Gaussian), all histograms of the model results are asymmetric. Although most of them are difficult to characterize, the time to failure (t_{fail}) seems to follow a lognormal distribution. Our tests show that if all $\theta_{i(i\neq j)}$ are kept constant (i.e., a single fixed value) and only θ_j varies, the distribution of t_{fail} is lognormal, for j = 1, 2, 3, 4. Although a linear dependence between $\log(t_{fail})$ and each θ_j is difficult to prove analytically, we can check numerically that $\log(t_{fail})$ varies roughly linearly with each parameter of the creep law since they graphically define a cloud of points with a linear trend. Therefore, since each θ_j follows a Gaussian distribution, the logarithm of the time to failure follows the same type of distribution as the product of Gaussians θ_j, and t_{fail} is expected to be lognormal, as observed (Figures 8 and 9).

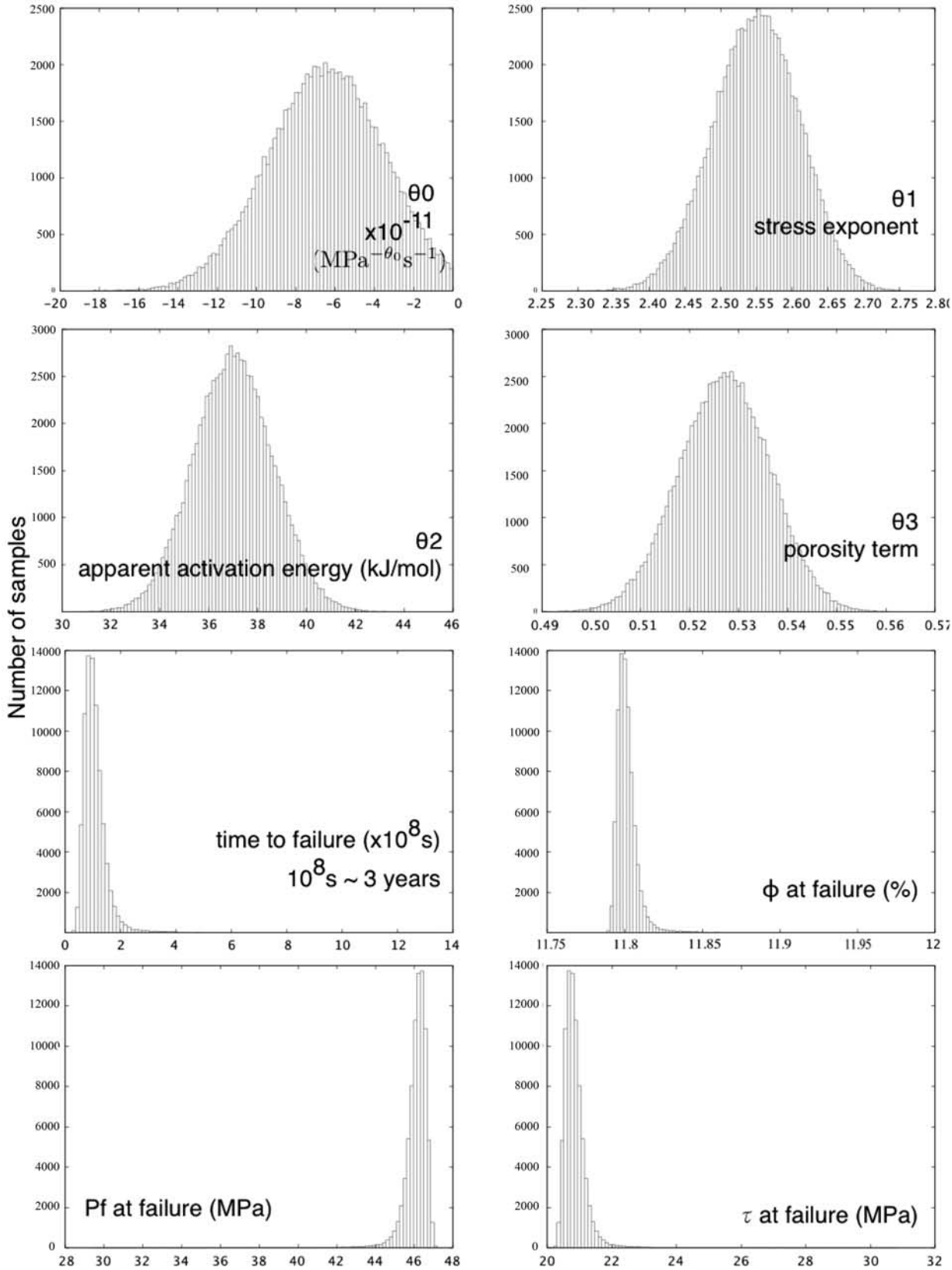

Figure 8. Histograms of the input parameters and the results for a fixed initial porosity of 12%. Although the creep parameters all follow a Gaussian, the results have asymmetric distributions. The creep parameters result from our inversion of the global data set of *Niemeijer et al.* [2002].

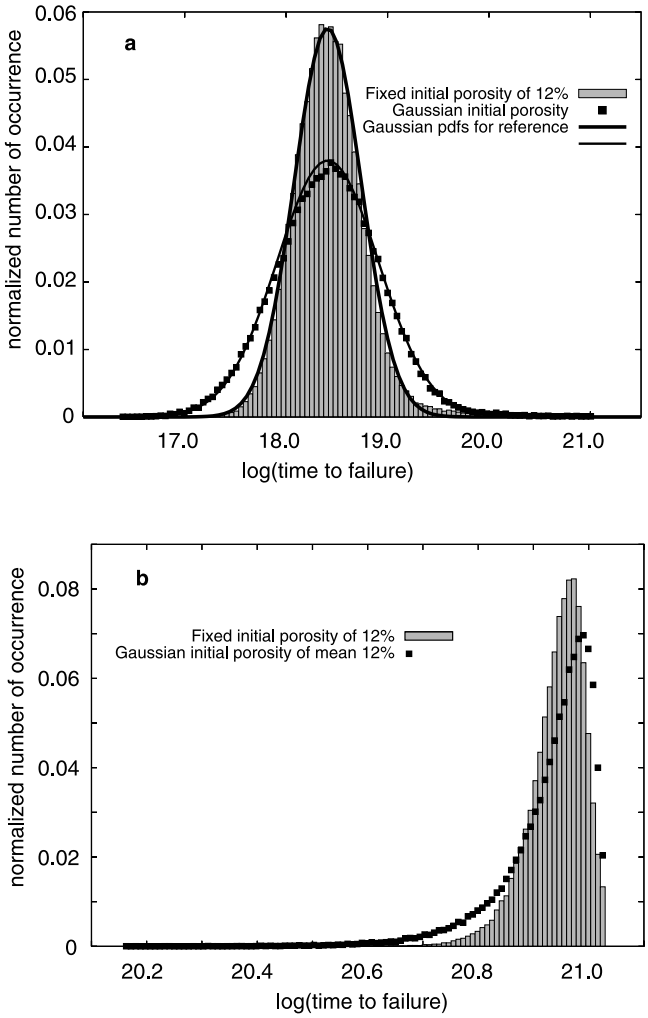

Figure 9. Comparison of the distributions of the log of time to failure for (1) a fixed initial porosity of 12% and (2) a random Gaussian porosity of mean 12% computed using samples for the creep parameters drawn from the pdf obtained for (a) the global data set and (b) the data set restricted to $0.5 \leq \phi/\phi_0 \leq 0.8$ of the *Niemeijer et al.* [2002] experiments. Figure 9a, both can be well approximated by Gaussians of about the same mean. This is not the case in Figure 9b. See details in Table 4.

[56] To further test the robustness of the asymmetry in time to failure, we now choose a Gaussian distribution for the initial porosity ϕ_t of mean 12% and standard deviation of 1%, truncated to keep values from 9 to 15% (99% confidence interval), and rerun our Monte Carlo analysis (using the same creep parameters inferred from the global *Niemeijer et al.* [2002] data set). The main conclusion remains, namely, that the time to failure is still lognormal. In log space, the two distributions have approximately the same mean (Figure 9). We can compute the 2σ and 3σ confidence intervals for each lognormal distribution from the parameters of the Gaussians in log space. We find that for the Gaussian ϕ_t (case 2) the 2σ confidence interval corresponds to the 3σ confidence interval for the fixed ϕ_t (case 1) (Table 4).

[57] We can also compute the marginal pdf of the time to failure using values for the creep parameters drawn from the pdf obtained by our inversion of the subset of the *Niemeijer et al.* [2002] data for $0.5 \leq \phi/\phi_0 \leq 0.8$. Since the covariance of $\{\theta\}$ is much larger, indicating larger variances and larger correlations between the creep parameters, we get a different shape for the distribution of time to failure (Figure 9b) and for all the other model results as well. In particular, the pdf of time to failure is not a lognormal distribution. Two properties still hold, though. First, model results for time to failure, ϕ, P_f and τ at failure have asymmetric marginal pdfs as for the analysis using the global data set inference results. Second, as shown in Figure 9b, the 2σ confidence interval of the time to failure computed with a Gaussian initial porosity of mean 12% and standard deviation 1% corresponds to the 3σ confidence interval of t_{fail} computed with a fixed initial porosity of 12%. However, the skewness of the distribution of time to failure is different from that of a lognormal distribution. Our experiments show that this change in skewness is related to the covariance between the creep parameters and not to their mean values (hence, not to the rate of shear stress increase relative to the rate of pore pressure increase). Indeed, we tested an hypothetical multivariate pdf with the mean creep parameters as inferred from the *Niemeijer et al.* [2002] restricted to $0.5 \leq \phi/\phi_0 \leq 0.8$ but with the covariance matrix obtained for the global data set, and we get a heavier tail for large times to failure (i.e., consistent with the form of a lognormal distribution). Finding the type of asymmetry therefore requires analysis of the nonlinear transform between the multidimensional Gaussian of the creep parameters and the pdf of the time to failure. This is beyond the scope of the present study.

[58] We can draw two main conclusions from the preceding analysis. First, in the case of mostly uncorrelated distributions for the creep parameters, the marginal pdf of the time to failure can be approximated by a lognormal distribution. This might allow one to solve the direct model without using a (computer intensive) Monte Carlo sampling technique by reparameterizing the problem (e.g., trying to solve for the logarithm of the time to failure). Second, we showed that not knowing precisely the porosity in the deformed core of a fault zone after an earthquake might not be a big impediment in the estimation of the time to failure (i.e., time of the next earthquake). Even though the variability of time to failure increases when we add this source of uncertainty, the mean values do not differ greatly, and the pdfs keep the same forms.

[59] A logical extension of this work would be to conduct a reparameterization of the problem working with Gaussians to allow us to derive the pdf of the time to failure semi-analytically. This would prove most useful when modeling interacting fault elements in a more complex rupture model.

6. Discussion and Implications

6.1. On the Analysis of Lab Data

[60] We developed a robust Bayesian inference scheme to help analyze and/or plan laboratory rock deformation experiments. Although we chose a simple creep compaction law for this analysis, similar inference schemes could be derived for a wide variety of deformation mechanisms and their corresponding creep laws. Indeed, the use of this

Table 4. Confidence Intervals for the Time to Failure for the Global Data Set of *Niemeijer et al.* [2002] Assuming a Fixed or a Gaussian Initial Porosity ϕ_0[a]

		Case 1 ϕ_0 = 12%	Case 2 ϕ_0 = Gaussian Around 12%
2σ	lower bound = $\exp(\nu)/\exp(\sigma)^2$	5.11×10^7 s	3.66×10^7 s
	upper bound = $\exp(\nu) \times \exp(\sigma)^2$	1.91×10^8 s	2.71×10^8 s
3σ	lower bound = $\exp(\nu)/\exp(\sigma)^3$	3.67×10^7 s	2.22×10^7 s
	upper bound = $\exp(\nu) \times \exp(\sigma)^3$	2.66×10^8 s	4.46×10^8 s

[a]The ν and σ represent the mean and the standard deviation of the Gaussian distributions in log space.

inference scheme to analyze lab experiments removes the need to compare strain rates at the same state, thus allowing the simultaneous use of the whole data set, leading to a more robust determination of the constitutive parameters. Although it is best to choose the appropriate creep law for the analysis of a particular data set before conducting the Bayesian inference (through microstructural observations or other means), the formal error analysis made possible by this Bayesian inference scheme allows one to evaluate the validity of a wide range of creep laws for any particular data set. An additional advantage of the method presented here is that the physical state of the sample does not have to be arbitrarily fixed in order to obtain the relevant constitutive parameters, since, if our assumed model is correct, then the time evolution of state is explicitly included in our analysis.

[61] We show on simulated data that despite the high degree of nonlinearity of the problem, we can retrieve accurate estimates of both the stress exponent and the activation energy, even when the porosity data are noisy. We also show that, whereas adding observation points and/or experiments reduces the uncertainty on all parameters, enlarging the range of temperature and/or effective stress conditions explored in a particular suite of experiments reduces the covariance between stress exponent and activation energy significantly, allowing these parameters to be determined with greater accuracy.

[62] When adapted to porosity-time series and applied to the hydrothermal quartz data of *Niemeijer et al.* [2002], our analysis suggests that this simple model does not capture all of the physics involved throughout the experiments, especially at high initial porosities (i.e., short elapsed times). However, for a subset of the data corresponding to a ratio of instantaneous porosity over initial porosity between 0.5 and 0.8 (i.e., the interval over which *Niemeijer et al.* [2002] focus their analysis), the 99% confidence regions for the stress exponent and the apparent activation energy agree with those obtained using conventional analysis at comparable compacted porosities (i.e., similar states). Our analysis also suggests that those mechanisms that have an activation energy lower than 49 kJ mol^{-1} or higher than 66 kJ mol^{-1} can be rejected at the 99% confidence level, given the assumed creep law.

[63] The value of 57.6 ± 2.6 kJ mol^{-1} for the apparent activation energy obtained using our Bayesian inference scheme is thus in agreement with the interpretation by *Niemeijer et al.* [2002] (based also on microstructural observations) that compaction creep was rate-limited by a dissolution-precipitation creep process, although the high stress exponents obtained in both their analyses and ours do not allow one to rule out a significant contribution from cataclasis and stress corrosion cracking over the range of porosities investigated.

[64] More comparisons between results published by the rock deformation community and those obtained via the type of methods presented here could lead to an enhanced understanding of the usefulness and limitations of lab data by modelers and, perhaps, the planning and execution of laboratory rock deformation experiments that were of the greatest possible use in modeling the earthquake source.

6.2. On the Integrative Bayesian Framework for Rupture Models

[65] We examined the influence of interseismic creep compaction on the time to failure using quantitative, semi-empirical compaction laws derived from laboratory experiments as a proxy for micromechanistic constitutive laws.

[66] We showed how we can propagate the uncertainties in creep compaction parameters through a deterministic (forward) model of both the pore pressure evolution and the rupture process to get the time to failure and conditions at failure.

[67] The ingredients of this forward model were rather simple and included undrained conditions, constant shear stress increase rate, and Coulomb failure criterion. However, the numerical integration scheme can accommodate more complex coupled differential equations, to include factors such as diffusion out of the fault zone, or time-dependent ''tectonic loading'' impacting both the normal stress and the shear stress.

[68] We show in the case of a shallow fault (3 km depth), that precise estimates of porosity right after an earthquake (within a bounded interval) may not be required to compute time to failure. Indeed, when the initial porosity varies between 9 and 15% around a mean of 12%, the 2σ confidence interval of the time to failure coincides with the 3σ confidence interval for a fixed ϕ_0 = 12%. This is true regardless of the ''quality'' of the estimates for the constitutive parameters obtained through analysis of lab compaction data of *Niemeijer et al.* [2002], encompassing both the uncorrelated posterior distribution of the creep parameters obtained with the global data set and the more correlated one obtained using the subset of porosities thought to best represent the creep compaction process.

[69] Using the Coulomb failure criterion in models such as that presented here shows that when the rate of shear stress increase is rather low compared to the rate of pore pressure increase, the time to failure will be controlled by the creep law. What our simulations allow us to compute is the variability of the time to failure. We show that in the situation where the pore pressure increase rate dominates the time evolution of the Coulomb failure stress, the pdf of

the time to failure is wide (i.e., time to failure will vary significantly with minor variations in compaction creep parameters) regardless of the precision with which the initial porosity or other variables can be estimated. This has important implications for applying physics-based models to predictions of earthquake recurrence rates. In addition, with the constitutive law that we chose to use in inverting the *Niemeijer et al.* [2002] creep data, in the undrained case and with a constant shear stress increase rate the marginal distributions of the time to failure are lognormal if the inferred stress exponent and apparent activation energy are almost uncorrelated. Again, this form of the time to failure pdf was not imposed in the model, but only reflects the interplay between the pdfs of the creep parameters, which proved to be Gaussian close to their optimum values, and the set of deterministic equations chosen to describe the evolution of fault zone fluid pressure, the shear stress loading rate, and the failure criterion.

[70] Our simple model using a single finite fault element seems to be well suited for integrative studies of small earthquakes with short recurrence intervals such as seen along the central San Andreas Fault, and the spatial and temporal interactions between these earthquakes. However, it is important to note that the creep law that we developed here may not be appropriate to the long time scales and large rupture dimensions appropriate to larger earthquakes.

[71] Our model is modular and the numerical methods used to solve coupled differential equations make it very flexible. More complicated behaviors, such as time-dependent friction, fluid diffusion out of the fault, time variations in fault-normal compressive stresses ($\dot{\sigma}_n \neq 0$), postseismic relaxation ($\dot{\tau} \neq$ constant) and other factors could therefore be incorporated. Future work could also include more sensitivity analyses to test the influence of variations in temperature, friction, fluid leakage out of the fault, and other parameters on pore pressure evolution and time to failure.

[72] In addition, we currently use a compaction law derived for the isotropic compaction of porous media between 10 and 30% porosity. Shear-enhanced compaction is therefore ignored. If data become available for a large range of porosities (e.g., down to 5%) under a deviatoric stress, we could apply the inference scheme used here with a different model to expand this modeling result to more realistic initial porosities and loading conditions. In particular, shear-enhanced compaction would release some of the shear stress accumulating on the fault, effectively reducing the shear stressing rate, while at the same time increasing the compaction rate and hence the rate of fluid pressure increase. The effect of these competing mechanisms on time to failure is difficult to predict without additional modeling.

[73] Finally, other attempts at deriving physically based probability density functions for time to failure or earthquake recurrence include works by *Matthews et al.* [2002] and *Ellsworth et al.* [1999]. They considered a fixed, seismic source loaded by steady tectonic forcing. They further assumed that it was rupturing in repeated occurrences of its characteristic earthquake. In *Matthews et al.*'s [2002] model, the loading of the system has two components, a constant rate component, and a stochastic component, that is defined as Brownian motion, or random walk (e.g., due to stress interaction between faults or other processes). An event occurs when the state variable (e.g., stress, strain or moment deficit) reaches a fixed threshold and the times between events are independent, identically distributed random variables. The steady loading uniformly increases the value of that state variable while the scale of the random walk controls the irregularity of the failure intervals. The distribution function of ''passage times'' across the failure threshold is known as the Brownian passage time (BPT) distribution. The state variable is a formal parameter of a point process model. The resulting BPT therefore potentially captures many sources of irregularity of earthquake times, including the stochastic nature of the accumulating tectonic stress but also time-dependent changes in fault strength caused by a compacting fluid-saturated fault zone with constant friction coefficient as long as they can be modeled by additive Brownian motion.

[74] In the context of our study, it is noteworthy that the BPT and the lognormal pdfs have very similar behaviors for times up to twice the mean time to failure [*Matthews et al.*, 2002]. However, they diverge at long times and have very different asymptotic failure rates: a finite rate for the BPT and a rate equal to 0 for the lognormal pdf.

[75] As discussed in section 5.3, from a technical stand point, knowing that the pdf of the time to failure in our model can be approximated by a lognormal distribution close to its optimum is enough to enable us to work on a reparameterization of the problem that allows solution of the problem analytically. However, it is obvious that in terms of seismic hazard assessment, this difference in asymptotic behavior becomes crucial.

[76] *Matthews et al.* [2002] showed in Table 1 of their appendix how difficult it was to discriminate between the two laws from synthetic catalogs containing 50 samples. This indicates that it will not be easy to discriminate between these two different laws using observations from actual earthquakes.

[77] In our model, since we can generate as large a number of samples as we want, we are currently investigating whether we can discriminate between a lognormal pdf and other time-to-failure models (BPT, Weibull, Gamma, etc.) for the time to failure that we generate.

6.3. On the Use of Bayesian Methods in the Solid Earth Sciences in General and for Seismic Hazard Assessment in Particular

[78] Although applications of Bayesian methods in the Earth sciences are still scarce compared to other fields, Bayesian methodologies have been used in several types of geophysical investigations. *Agostinelli and Rotondi* [2003] present a detailed description of the methodology as applied to model selection for seismic hazard assessment. They use Bayesian Belief Networks to analyze the stochastic dependence between several types of observations recorded in a parametric catalogue of damaging earthquakes in Italy, namely, the time since the last earthquake, the time to the subsequent event, and the maximum (epicentral) intensity of the event (discrete variables). Bayesian inference has also been used to incorporate prior knowledge in an inversion scheme where a deterministic model links the random variables [*Tarantola and Valette*, 1982; *Mosegaard and Tarantola*, 2002]. A recent application by *Johnson and Segall* [2004], for example, uses Bayesian inference to

invert contemporary and post-1906 velocity fields for the rheology of the lithosphere and asthenosphere in northern and southern California. Finally, Bayesian techniques can also provide a powerful data integration (fusion) tool. *Ezzedine et al.* [1999] present a stochastic Bayesian approach for combining well logs and geophysical surveys to enhance the resolution of subsurface characterization.

[79] Quantifying seismic hazard requires working with data sets obtained using widely varying techniques with different spatial or temporal resolutions and precision, analyzed in the light of, or fed into, competing conceptual and numerical models of interacting physical or chemical processes. All of the aforementioned Bayesian methods could therefore help solve parts of this very complicated problem in a consistent way. In addition, combining these partial analyses into a unified model would be made easier by the use of a rigorous illustration of the relationships between all its components using the types of graphical models presented here. Finally, in the recent efforts to quantify uncertainties in seismic hazard assessment [see *Field et al.*, 2003], two main sources of errors were identified. The aleatory uncertainties are related to the inherent variability in any type of measurement or observation; these are the uncertainties we quantified and propagated in the present study. In contrast, the epistemic uncertainties arise when one is trying to explain a data set with a wrong model. To reduce this source of uncertainty, we again strongly advocate the use of Bayesian frameworks, for the inversion of lab or field data, in our case as a means of correctly identifying the underlying physics and relevant constitutive law. As previously mentioned, this would involve the extension of our present work to include a step of model selection in which the ''scores'' of several competing creep models are compared. The model that can best explain the data is thus identified and can then be used for all follow-up studies aiming at the integration of lab data into fault modeling.

Appendix A: Mathematical Formulation of the Inference Scheme

[80] The reparameterizatioin we use is

$$\lambda' = -\frac{1}{\theta_3}\log(\theta_3\gamma'), \quad \mu = \frac{1}{\theta_3} \quad \text{and} \qquad \Theta = F(\theta) = \{\log(-\theta_0)/\theta_3, \theta_1/\theta_3, \theta_2/\theta_3, 1/\theta_3\} \tag{A1}$$

which reduces equation (2) to a new expression, with the new constants $k = \{\log \sigma_{\text{eff}}, 1/(RT)\}$:

$$f(\varphi_0, t) = -\mu \log\left(t\, e^{-\lambda'/\mu} + e^{-\varphi_0/\mu}\right) \tag{A2}$$

where

$$\lambda' = h(\Theta) = -\Theta_0 - k_1\Theta_1 + k_2\Theta_2 + \Theta_3 \log\Theta_3 \quad \text{and} \quad \mu \equiv \Theta_3 \tag{A3}$$

[81] For each experiment n, the joint probability of the variables of step A is

$$P\left(\varphi_0, \{\phi^i, \phi^i_{\text{obs}}\}, \lambda', \nu, m\right) = P(\varphi_0)P(m)\prod_i P\left(\phi^i_{\text{obs}}|\phi^i\right) \cdot P\left(\phi^i|\varphi_0, \lambda', \nu, m\right) \tag{A4}$$

where i spans the number of observations for each experiment and $P(\varphi_0)$ and $P(m)$ are the a priori constraints (prior) on φ_0 and on the model m, respectively.

[82] For step B, the joint probability is given by

$$P\left(\Theta, \{\lambda'^n, \nu^n, \lambda'^n_{\text{obs}}, \nu^n_{\text{obs}}\}, m\right) = P(\Theta)P(m)\prod_n P(\lambda'^n, \nu^n|\Theta, m) \cdot P\left(\lambda'^n_{\text{obs}}, \nu^n_{\text{obs}}|\lambda'^n, \nu^n, m\right) \tag{A5}$$

In this study, all the model parameters were introduced in reference to the same model. To simplify the equations, we will therefore omit m and write $P(\phi^i|\varphi_0, \lambda', \nu)$ instead of $P(\phi^i|\varphi_0, \lambda', \nu, m)$.

[83] Each expression can be greatly simplified by noting that there are deterministic relationships between some of the variables, such as f (equation (A2)) between ϕ^i and (φ_0, t^i, λ', ν), or h (equation (A3)) between Θ and λ'. The pdf $P(\phi^i|\varphi_0, \lambda', \nu)$ is simply the Dirac distribution $\delta(\phi^i - f(\varphi_0, t^i, \lambda', \nu))$. Further simplification is achieved by assuming that the observations (ϕ^i_{obs} in step A) follow a Gaussian distribution around their mean (e.g., ϕ^i) with a variance (e.g., σ^2).

[84] For both steps, there are more nodes in the graphs than just the parameters and the observations. However, the posterior pdfs we are looking for in steps A and B are proportional not to the complete joint pdfs but rather to the corresponding restricted joint pdfs $P(\lambda', \nu, \{\phi^i_{\text{obs}}\})$ and $P(\Theta, \{\lambda'^n_{\text{obs}}, \nu^n_{\text{obs}}\})$, respectively. The restricted joint pdfs are simply the integral of the complete joint pdfs over all possible values of the parameters we are not interested in (corresponding on the graph to the intermediate nodes between the observations and the parameters we want to infer, e.g., for step A, φ_0 and ϕ^i). This is the marginalization step.

[85] For step A, the complete joint pdf is

$$P\left(\varphi_0, \{\phi^i, \phi^i_{\text{obs}}\}, \lambda', \nu\right) = P(\varphi_0)\prod_i \frac{1}{\sigma\sqrt{2\pi}} \cdot \exp\left(-\frac{1}{2}\left(\frac{\phi^i_{obs} - \phi^i}{\sigma}\right)^2\right) \cdot \delta\left(f(\varphi_0, t^i, \lambda', \nu) - \phi^i\right) \tag{A6}$$

so that, after switching the product and the integral, the restricted pdf becomes simply

$$P\left(\{\phi^i_{\text{obs}}\}, \lambda', \nu\right) = \int_{\varphi_0} P(\varphi_0)\prod_i \frac{1}{\sigma\sqrt{2\pi}} \cdot \exp\left(-\frac{1}{2}\left(\frac{\phi^i_{obs} - f(\varphi_0, t^i, \lambda', \nu)}{\sigma}\right)^2\right) d\varphi_0 \tag{A7}$$

[86] Once we reduced the dimensionality of the problem, the last step of the inference is the optimization which is achieved by approximating the posterior pdf by a Gaussian around its mode (i.e., making the Laplace approximation [see *MacKay*, 2003]). Maximizing a posterior pdf P is equivalent to minimizing the energy $U = -\log(P)$. The minimum of U provides the optimal values of the parameters and the second derivatives of U at the optimum give the uncertainties.

[87] To solve step A, we use the fact that, thanks to the reparameterization, $U(\{\phi^i_{\text{obs}}\}, \lambda', \nu, \varphi_0)$ is approximately quadratic with respect to λ' and ν close to the optimum. We couple the marginalization and the optimization by performing iteratively the several steps that can be characterized as Newton descent. For given initial values for λ' and ν we compute the optimal φ_0 using a line search. We then compute the first and second derivatives of U with respect to λ' and ν using the (locally) optimal φ_0. At iteration k + 1, the updated values for λ' and ν are then

$$\lambda'_{k+1} = \lambda'_k - \left(\frac{\partial^2 U}{\partial \nu^2}\frac{\partial U}{\partial \lambda'} - \frac{\partial^2 U}{\partial \lambda' \partial \nu}\frac{\partial U}{\partial \nu}\right)/\det \tag{A8}$$

$$\nu_{k+1} = \nu_k - \left(\frac{\partial^2 U}{\partial \lambda'^2}\frac{\partial U}{\partial \nu} - \frac{\partial^2 U}{\partial \nu \partial \lambda'}\frac{\partial U}{\partial \lambda'}\right)/\det, \tag{A9}$$

where $\det = \frac{\partial^2 U}{\partial \nu^2}\frac{\partial^2 U}{\partial \lambda'^2} - \frac{\partial^2 U}{\partial \nu \partial \lambda'}\frac{\partial^2 U}{\partial \lambda' \partial \nu}$. For these values of λ' and ν, a new optimal φ_0 is computed. After a few iterations, the λ' and ν converge to the actual optimum and the second derivatives of U at the optimum (in φ_0, λ', and ν) provide the entries of the inverse of the covariance matrix.

[88] Step B is identical to that described by *Fitzenz et al.* [2005]. Let us just note that once the optimal $\{\Theta\}$ and their inverse covariance matrix B are found, an additional step is needed to get the solution in terms of the constitutive parameters. Let us denote by F the transform such that $\Theta = F(\theta)$, as specified by equation (A1). Let J denote the Jacobian matrix of the transform (i.e., the matrix of derivatives of Θ_j with respect to θ_l). We make a Laplace approximation, considering the multidimensional pdf of θ as a multivariate Gaussian close to its optimum. Then we can write the final result, where J is evaluated at the optimum, as

$$\begin{aligned} P\left(\theta \middle| \left\{\left\{\phi^i_{obs}\right\}^n\right\}\right) &\simeq P\left(\theta \middle| \left\{\lambda^n_{obs}, \nu^n_{obs}\right\}\right) \\ &\simeq G_\theta\left(F^{-1}\left(\hat{\Theta}\right), \left(J^T B J\right)^{-1}\right) \end{aligned} \tag{A10}$$

where $G_\theta\,[F^{-1}(\hat{\Theta}), (J^T B J)^{-1}]$ is the multivariate Gaussian distribution of θ of mean value $F^{-1}(\hat{\Theta})$ and of covariance matrix $(J^T B J)^{-1}$.

[89] **Acknowledgments.** The authors want to thank André Niemeijer and Chris Spiers for sharing their creep data and for insightful discussions. Many thanks to Andy Michael, Nick Beeler, Andreas Kronenberg, Steve Karner, and an anonymous Associate Editor for their helpful comments and suggestions. This research was supported by the USGS Earthquake Hazards Reduction Program and by the Southern California Earthquake Center. SCEC is funded by NSF Cooperative Agreement EAR-0106924 and USGS Cooperative Agreement 02HQAG0008. This is SCEC contribution 1073. D. F. is currently supported by a Marie Curie Reintegration Grant via a CNRS contract.

References

Agostinelli, C., and R. Rotondi (2003), Using bayesian belief networks to analyse the stochastic dependence between interevent time and size of earthquakes, *J. Seismol.*, *7*, 281–299.

Bernardo, J., and A. Smith (1994), *Bayesian Theory*, Ed. John Wiley, Hoboken, N. J.

Bos, B., C. J. Peach, and C. J. Spiers (2000), Frictional-viscous flow of simulated fault gouge caused by the combined effects of phyllosilicates and pressure solution, *Tectonophysics*, *327*(3–4), 173–194.

Byerlee, J. (1978), Friction of rocks, *Pure Appl. Geophys.*, *116*(4–5), 615–626.

Chester, J., S. Lenz, F. M. Chester, and R. Lang (2004), Mechanisms of compaction of quartz sand at diagenetic conditions, *Earth Planet. Sci. Lett.*, *220*(3–4), 435–451.

Dewers, T., and A. Hajash (1995), Rate laws for water-assisted compaction and stress-induced water-rock interaction in sandstones, *J. Geophys. Res.*, *100*, 13,093–13,112.

Ellsworth, W. L., M. Matthews, R. M. Nadeau, S. P. Nishenko, P. A. Reasenberg, and R. W. Simpson (1999), A physically-based earthquake recurrence model for estimation of long-term earthquake probabilities, *U. S. Geol. Surv. Open File Rep.*, *99-522*.

Ezzedine, S., Y. Rubin, and J. Chen (1999), Bayesian method for hydrogeological site characterization using borehole and geophysical survey data: Theory and application to the lawrence livermore national laboratory superfund site, *Water Resour. Res.*, *35*(9), 2671–2683.

Field, E. H., T. H. Jordan, and C. A. Cornell (2003), OpenSHA: A developing community-modeling environment for seismic hazard analysis, *Seismol. Res. Lett.*, *74*, 406–419.

Fitzenz, D. D., and S. A. Miller (2003), Fault compaction and overpressured faults: Results from a 3D model of a ductile fault zone, *Geophys. J. Int.*, *155*, 111–125.

Fitzenz, D., A. Jalobeanu, S. H. Hickman, and N. Sleep (2005), Integrating laboratory compaction data with numerical fault models: A Bayesian framework, in *25th International Workshop on Bayesian Inference and Maximum Entropy Methods in Science and Engineering, San Jose, California, August 2005, Melville, N.Y, AIP Conf. Proc.*, *803*, 483–490.

Hickman, S. H., and B. Evans (1992), Growth of grain contacts in halite by solution transfer: Implications for diagenesis, lithification, and strength recovery, in *Fault Mechanics and Transport Properties of Rocks*, *Int. Geophys. Ser.*, vol. 51, pp. 253–280, Academic, San Diego, Calif.

Johnson, K. M., and P. Segall (2004), Viscoelastic earthquake cycle models with deep stress-driven creep along the San Andreas fault system, *J. Geophys. Res.*, *109*, B10403, doi:10.1029/2004JB003096.

Jordan, M. I. (2004), Graphical models, *Stat. Sci.*, *19*, 140–155.

Jordan, M. I., and Y. Weiss (2002), Graphical models: Probabilistic inference, in *Handbook of Neural Networks and Brain Theory*, 2nd ed., edited by M. Arbib, MIT Press, Cambridge, Mass.

MacKay, D. J. C. (1998), Choice of basis for Laplace approximation, *Mach. Learn.*, *33*(1), 77–86.

MacKay, D. J. C. (2003), *Information Theory, Inference, and Learning Algorithms*, Cambridge Univ. Press, New York.

Matthews, M., W. L. Ellsworth, and P. A. Reasenberg (2002), A Brownian model for recurrent earthquakes, *Bull. Seismol. Soc. Am.*, *92*(6), 2233–2250.

Mosegaard, K., and A. Tarantola (2002), Probabilistic approach to inverse problems, in *International Handbook of Earthquake and Engineering Seismology, Part A*, pp. 237–265, Academic, San Diego, Calif.

Muhuri, S., T. A. Dewers, J. T. E. Scott, and Z. Reches (2003), Interseismic fault strengthening and earthquake-slip instability: Friction or cohesion?, *Geology*, *31*, 881–884.

Niemeijer, A., C. J. Spiers, and B. Bos (2002), Compaction creep of quartz sand at 400–600°C: Experimental evidence for dissolution-controlled pressure solution, *Earth Planet. Sci. Lett.*, *195*, 261–275.

Rutter, E. H., and P. Wanten (2000), Experimental study of the compaction of phyllosilicate-bearing sand at elevated temperature and with controlled pore water pressure, *J. Sediment. Res.*, *70*, 107–116.

Schutjens, P. M. (1991), Experimental compaction of quartz sand at low effective stress and temperature conditions, *J. Geol. Soc. London*, *148*, 527–539.

Segall, P., and J. R. Rice (1995), Dilatancy, compaction, and slip instability of a fluid-infiltrated fault, *J. Geophys. Res.*, *100*, 22,155–22,171.

Spiers, C. J., P. M. T. M. Schutjens, R. H. Brezesowsky, C. J. Peach, J. L. Liezenberg, and H. J. Zwart (1990), Experimental determination of constitutive parameters governing creep of rocksalt by pressure solution, in *Deformation Mechanisms, Rheology and Tectonics*, edited by R. J. Knipe and E. H. Rutter, *Geol. Soc. Spec. Publ.*, *54*, 215–227.

Stein, R. S., A. A. Barka, and J. H. Dieterich (1997), Progressive failure on the North Anatolian fault since 1939 by earthquake stress triggering, *Geophys. J. Int.*, *128*, 594–604.

Tarantola, A., and B. Valette (1982), Generalized nonlinear inverse problems solved using the least squares criterion, *Rev. Geophys.*, *20*, 219–232.

Williams, C. F., F. V. Grubb, and S. P. Galanis Jr. (2004), Heat flow in the SAFOD pilot hole and implications for the strength of the San Andreas Fault, *Geophys. Res. Lett.*, *31*, L15S14, doi:10.1029/2003GL019352.

D. D. Fitzenz, Institut de Physique du Globe, EOST, 5 rue René Descartes, F-67084 Strasbourg Cedex, France. (delphine.fitzenz@eost.u-strasbg.fr)

S. H. Hickman, U.S. Geological Survey, 345 Middlefield Road, MS 977 Menlo Park, CA 94025, USA. (hickman@usgs.gov)

A. Jalobeanu, LSIIT (UMR 7005 CNRS-ULP) ENSPS-Parc d'Innovation, Bd Sébastien Brant BP 10413, F-67412 Illkirch Cedex, France. (jalobeanu@lsiit.u-strasbg.fr)